

See discussions, stats, and author profiles for this publication at: <https://www.researchgate.net/publication/259537605>

Alkylation Effects in Lanthanide Complexes Involving Tetrathiafulvalene Chromophores: Experimental and Theoretical Correlation between Magnetism and Near-Infrared Emission

ARTICLE in *BERICHTE DER DEUTSCHEN CHEMISCHEN GESELLSCHAFT* · JANUARY 2014

Impact Factor: 2.94 · DOI: 10.1002/ejic.201301358

CITATIONS

15

READS

37

10 AUTHORS, INCLUDING:



Fabrice Pointillart

Université de Rennes 1

73 PUBLICATIONS 1,282 CITATIONS

SEE PROFILE



Boris Le Guennic

Université de Rennes 1

137 PUBLICATIONS 2,368 CITATIONS

SEE PROFILE



Olivier Cador

Université de Rennes 1

126 PUBLICATIONS 2,460 CITATIONS

SEE PROFILE



Olivier Maury

Ecole normale supérieure de Lyon

169 PUBLICATIONS 3,435 CITATIONS

SEE PROFILE

DOI:10.1002/ejic.201301358

Alkylation Effects in Lanthanide Complexes Involving Tetrathiafulvalene Chromophores: Experimental and Theoretical Correlation between Magnetism and Near-Infrared Emission

Goulven Cosquer,^[a] Fabrice Pointillart,^{*,[a]} Julie Jung,^[a] Boris Le Guennic,^{*,[a]} Stéphane Golhen,^[a] Olivier Cador,^[a] Yannick Guyot,^[b] Alain Brenier,^[b] Olivier Maury,^{*,[c]} and Lahcène Ouahab^[a]

Keywords: Alkylation / Lanthanides / Magnetic properties / Luminescence / Ab initio calculations

Mononuclear complexes with the formula $[\text{Ln}(\text{hfac})_3(\text{L}^1)]$ and $[\text{Ln}(\text{hfac})_3(\text{L}^2)]$ with $\text{hfac}^- = 1,1,1,5,5,5$ -hexafluoroacetylacetonate, $\text{L}^1 = 2$ -{4,5-[4,5-bis(propylthio)tetrathiafulvalenyl]-1*H*-benzimidazol-2-yl}pyridine and $\text{L}^2 = 2$ -{1-methylpyridyl-4,5-[4,5-bis(propylthio)tetrathiafulvalenyl]-1*H*-benzimidazol-2-yl}pyridine are reported for $\text{Ln} = \text{Y}^{\text{III}}$, Er^{III} and Yb^{III} . The X-ray structures reveal that the $\text{Ln}(\text{hfac})_3$ moieties are coordinated to the bidentate 1-(2-pyridylmethyl)-benzimidazole acceptor. The coordination polyhedron is described as a more or less distorted triangular dodecahedron prism (D_{2d} symmetry), depending on the degree of alkylation of the ligand. The influence of this distortion on the magnetic and photophysical properties is determined by the fit of the static magnetic measurements and luminescence spectra. Irradiation of the lowest-energy intraligand charge transfer (ILCTs) bands (21740 cm^{-1}) induces the metal-centred

$^4\text{I}_{13/2} \rightarrow ^4\text{I}_{15/2}$ and $^2\text{F}_{5/2} \rightarrow ^2\text{F}_{7/2}$ luminescence for the Er^{III} and Yb^{III} complexes, respectively. The alkylation enhances both the intensity and lifetime of the Yb^{III} luminescence. The Er^{III} luminescence can be sensitised by the antenna effect, whereas the Yb^{III} luminescence could involve a photoinduced electron transfer (PET). Finally, the evolution of the Yb^{III} luminescence spectra shape due to the alkylation is directly correlated to the energy splitting of the M_J states that stem from the $^2\text{F}_{7/2}$ multiplet ground state. Ab initio calculations give evidence of the nature of the M_J ground state as well as the orientation of the associated magnetic anisotropy axis (i.e., the one that lies along the less electronegative direction). The key role of the imidazole proton of L^2 is highlighted. The calculated energy splitting of the $^2\text{F}_{5/2}$ multiplet state perfectly matches the emission lines.

Introduction

Lanthanide coordination complexes are fascinating objects owing to their peculiar magnetic and luminescent properties. From a magnetic point of view, such molecules present large magnetic moments and anisotropy^[1] that make them good candidates—sometimes in association with transition-metal ions—for the design of magnetic materials^[2] such as single-molecule magnets (SMMs).^[3] The latter objects exhibit a memory effect at the molecular scale and

thus present potential applications in quantum computing^[4] and spintronic devices.^[5] From a spectroscopic point of view, the $4f^n$ electronic configuration generates a large number of electronic levels, the energies of which are well-defined and characteristic of each given lanthanide ion. In consequence, lanthanide ions exhibit specific, line-shape f – f emissions, which cover a large spectroscopic range from the visible to the near-infrared (NIR). These transitions are Laporte-forbidden,^[6] which results in very long-lived excited states. These unique luminescence properties combined with the development of lanthanide coordination chemistry have generated new applications in material science for OLEDs,^[7] in bioimaging, for sensing,^[8] in time-resolved luminescent immunoassays^[9] or time-resolved microscopy.^[10] Nevertheless, since lanthanide ions possess very small molar absorption coefficients, it is necessary to use other processes than a direct excitation of the weak f – f absorption bands to efficiently populate the lanthanide excited states. The sensitisation can be efficiently achieved by an indirect energy/electron transfer from an organic ligand

[a] Institut des Sciences Chimiques de Rennes, UMR 6226 CNRS, Université de Rennes 1, 263 Avenue du Général Leclerc, 35042 Rennes CEDEX, France
E-mail: fabrice.pointillart@univ-rennes1.fr
<http://www.scienceschimiques.univ-rennes1.fr>

[b] Université Claude Bernard Lyon 1, Institut Lumière Matière, UMR 5306 CNRS-Université Lyon 1, 10 rue Ada Byron, 69622 Villeurbanne CEDEX, France

[c] Laboratoire de Chimie, UMR 5182 CNRS-ENS Lyon-Université Lyon 1, 46 Allée d'Italie, 69364 Lyon Cedex 07, France

Supporting information for this article is available on the WWW under <http://dx.doi.org/10.1002/ejic.201301358>.

that acts as an antenna. Three mechanisms are usually reported that involve either (1) a triplet excited-state sensitisation process, (2) an induced triplet metal-to-ligand charge transfer (MLCT) or (3) a singlet excited-state pathway that involve intraligand charge-transfer (ILCT) excitations.^[11] In particular, the latter process is appropriate for the sensitisation of the visible Eu^{III} luminescence and NIR emitters such as Nd^{III} , Er^{III} and Yb^{III} .^[12] It was mainly stimulated for practical reasons (glass transparency, reduction of photodamage) and by the emergence of applications in molecular nonlinear optics (NLO).^[13]

In a first approximation, the sharp lanthanide emission bands are assigned to transitions from the emitting state to the various J levels of the ground state. Interestingly, each J level is further split into M_J states due to crystal-field effects ($10\text{--}100\text{ cm}^{-1}$) that can be detected by well-resolved emission spectroscopy. It is worth noting that the same energy splitting is responsible for the thermal variation of the magnetic susceptibility.

In other words, the energy splitting of the M_J states of the multiplet ground state is the origin of both the luminescence contributions and thermal variation of the magnetic susceptibility for a mononuclear complex. In this context, we recently proposed to use the lanthanide luminescence spectroscopy as a tool to probe the energy splitting of the M_J states of the multiplet ground state to fully rationalise molecular magnetism results. To that end, we focused on Yb^{III} derivatives since this element is known to present a single luminescence transition ($^2\text{F}_{5/2} \rightarrow ^2\text{F}_{7/2}$) and is therefore well suited to establish magnetism/luminescence correlation.^[14] Similar approaches were undertaken almost concomitantly by other groups on Tb or Dy derivatives that featured more complex emission spectra.^[15]

In the present contribution, the influence of the ligand substitution on both magnetic and luminescence behaviours is investigated. To that end, two families, $[\text{Ln}(\text{hfac})_3(\text{L}^1)]$ and $[\text{Ln}(\text{hfac})_3(\text{L}^2)]$ with $\text{hfac}^- = 1,1,1,5,5,5\text{-hexafluoroacetylacetonate}$, non-alkylated $\text{L}^1 = 2\text{-}\{4,5\text{-}[4,5\text{-bis}(\text{propylthio})\text{-tetra-thiafulvalenyl}]\text{-}1H\text{-benzimidazol-2-yl}\}\text{pyridine}$ and alkylated $\text{L}^2 = 2\text{-}\{1\text{-methylpyridyl-}4,5\text{-}[4,5\text{-bis}(\text{propylthio})\text{-tetra-thiafulvalenyl}]\text{-}1H\text{-benzimidazol-2-yl}\}\text{pyridine}$ (Scheme 1), were prepared for $\text{Ln}^{\text{III}} = \text{Y}$, Er and Yb ions and fully characterised. For the Yb^{III} derivatives, a direct correlation be-

tween the emission and magnetic properties is proposed on the basis of both experimental and theoretical points of view.

Results and Discussion

Synthesis

The two ligands L^1 and L^2 were previously obtained in a single synthetic step.^[16] The ligand L^1 was obtained by the direct condensation reaction between the 2-pyridine-carboxaldehyde and the 5,6-diamino-2-[4,5-bis(propylthio)-1,3-dithio-2-ylidene]benzo[*d*]-1,3-dithiole,^[17] whereas ligand L^2 was surprisingly obtained by means of a Cannizzaro reaction. With this original synthetic route, the (benzimidazol-2-yl)pyridine acceptor was (1) functionalised by a tetrathiafulvalene donor and (2) alkylated in the case of L^2 . In a successive step, the two ligands were coordinated by the $\text{Ln}(\text{hfac})_3 \cdot 2\text{H}_2\text{O}$ precursors ($\text{Ln} = \text{Y}^{\text{III}}$, Er^{III} and Yb^{III}), thus giving rise to the complexes $[\text{Ln}(\text{hfac})_3(\text{L}^n)]$ ($n = 1$ and 2).

Crystal Structure Analysis: $[(\text{L}^1)\text{Ln}(\text{hfac})_3]$ with $\text{Ln} = \text{Y}^{\text{III}}$ (1), Er^{III} (2) and Yb^{III} (3)

These three compounds are isostructural, and only the structure of **3** is described. The respective values for **1** and **2** are given in square brackets. The compounds crystallise in the triclinic $P\bar{1}$ (no. 2) space group (Table 5). An ORTEP view of **3** is depicted in Figure 1 (Figures S1 and S2 in the Supporting Information for **1** and **2**, respectively). It is composed of one molecule of L^1 and one $\text{Yb}(\text{hfac})_3$ [$\text{Y}(\text{hfac})_3$, $\text{Er}(\text{hfac})_3$] unit (Figure 1).

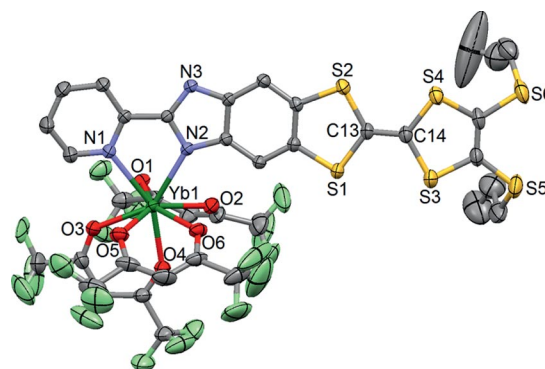
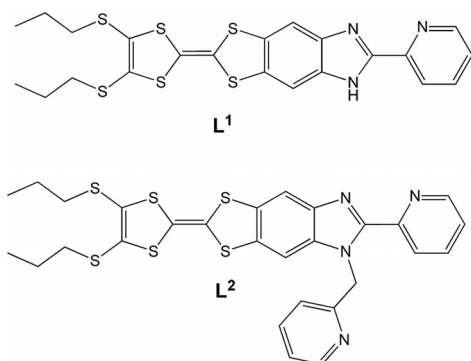


Figure 1. ORTEP view of the asymmetric unit of **3**. Thermal ellipsoids are drawn at 30% probability. Hydrogen atoms are omitted for clarity.

The Yb^{III} (Y^{III} , Er^{III}) ion is surrounded by six oxygen atoms and two nitrogen atoms that belong to three hfac^- ligands and one L^1 ligand. The lanthanide ion is coordinated to the pyridine and imidazole moieties, whereas the second nitrogen atom of the latter remains protonated. The average Yb–O distances are shorter [$2.296(5)\text{ \AA}$, $2.336(4)\text{ \AA}$, $2.330(5)\text{ \AA}$] than the average Yb–N distances [$2.448(5)\text{ \AA}$, $2.500(4)\text{ \AA}$, $2.476(5)\text{ \AA}$] (Table 1) due to the



Scheme 1. Schematic representation of ligands L^1 and L^2 .

Table 1. Selected bond lengths [Å] for complexes 1–6.

	1	2	3	4	5	6
Ln1–N1	2.546(4)	2.534(5)	2.511(4)	2.513(4)	2.496(4)	2.480(5)
Ln1–N2	2.453(4)	2.418(5)	2.403(4)	2.444(4)	2.431(4)	2.416(4)
Ln1–O1	2.369(4)	2.365(5)	2.343(4)	2.308(4)	2.291(4)	2.288(4)
Ln1–O2	2.382(4)	2.371(5)	2.361(4)	2.378(4)	2.376(4)	2.278(5)
Ln1–O3	2.352(4)	2.343(5)	2.326(4)	2.379(4)	2.370(4)	2.237(5)
Ln1–O4	2.298(4)	2.289(5)	2.267(4)	2.284(4)	2.273(4)	2.348(5)
Ln1–O5	2.310(4)	2.312(5)	2.283(4)	2.319(4)	2.306(5)	2.370(4)
Ln1–O6	2.306(3)	2.300(5)	2.281(4)	2.317(4)	2.314(4)	2.254(4)
C13–C14	1.343(7)	1.358(9)	1.341(7)	1.345(7)	1.343(8)	1.338(8)

oxophilic character of the $\text{Ln}(\text{hfac})_3$ Lewis acid. It is worth noting that the Ln–N bond lengths that involve the coordination with the 2-pyridine are longer than the Ln–N that involves the coordination with the imidazole. That is due to the difference in Lewis base character and steric hindrance between the 2-pyridine and imidazole rings. The arrangement of the ligands leads to a distorted coordination polyhedron around the lanthanide ions. This distortion is visualised by continuous shape measures (CShMs) performed with SHAPE 2.1.^[18] Table 2 collects CShMs for 1–3 for three different polyhedra: square antiprism, triangular dodecahedron and biaugmented trigonal prism. The lower the CShM, the closer the real polyhedron is to the ideal arrangement. Clearly, the coordination polyhedra of 1–3 are better described by D_{2d} symmetry but are still close to C_{2v} .

Table 2. SHAPE analysis of the coordination polyhedra around Ln1 in complexes 1 to 6.

	CShM _{SAPR-8} (square antiprism) D_{4d}	CShM _{TDD-8} (triangular dodecahedron) D_{2d}	CShM _{BTPR-8} (biaugmented trigonal prism) C_{2v}
1	1.963	1.104	1.399
2	1.902	1.074	1.323
3	1.887	1.016	1.383
4	1.215	1.138	1.547
5	1.175	1.095	1.505
6	1.240	1.020	1.471

The C13–C14 central bond length of the tetrathiafulvalene (TTF) moieties [1.341(7) Å, 1.343(7) Å, 1.358(9) Å] attests the neutrality of L^1 in 3 [1, 2]. In the crystal, dimers of molecules are formed through hydrogen bonds {N3–H3...O1 = 2.094(4) Å [2.094(4) Å, 2.094(4) Å]} between the protonated imidazole ring and the O1 atom of the neighbouring molecule. Thus the benzimidazole-2-pyridine of the two neighbouring molecules generates intermolecular acceptor–acceptor (A–A) interactions. Each of these dimers performs “head-to-tail” π – π stacking with the neighbouring molecule through intermolecular donor–acceptor (D–A) interactions. The combination of the intermolecular A–A and D–A interactions leads to the formation of a one-dimensional organic network along the *a* axis (Figure 2, a).

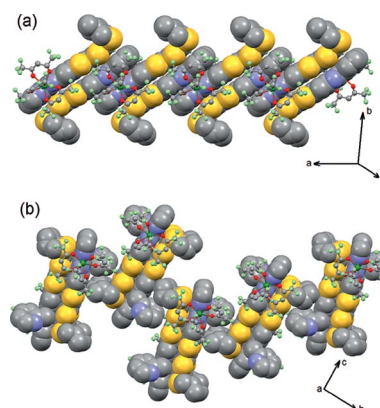


Figure 2. (a) Crystal packing of 3 highlighting the one-dimensional organic network (spacefill representation). (b) Crystal packing of 6 highlighting the dimerisation of the molecules.

2-[1-Methylpyridyl-4,5-[4,5-bis(propylthio)tetrathiafulvalenyl]-1H-benzimidazol-2-yl]pyridine (L^2)

The ligand crystallises in the triclinic $P\bar{1}$ (no. 2) space group (Table 5). An ORTEP view of L^2 is depicted in Figure 3. The TTF core is planar, whereas the planes formed by the pyridine ring and the benzimidazole moiety make an angle of 13.0(1)°. This differs significantly from the X-ray structure of $\text{L}^{[17]}$ with (1) a boat conformation of the TTF core and (2) the pyridine–benzimidazole acceptor that lies in the same plane as the TTF fragment. Both the methyl-2-

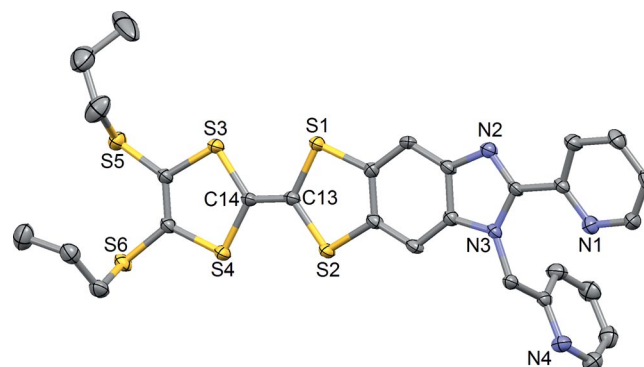


Figure 3. ORTEP view of the asymmetric unit of L^2 . Thermal ellipsoids are drawn at 50% probability. Hydrogen atoms are omitted for clarity.

pyridine arm and the benzimidazole-2-pyridine moiety interact [$C-H25\cdots N3 = 2.583(3) \text{ \AA}$ and $C-H23B\cdots N1 = 2.424(3) \text{ \AA}$]. The crystal packing reveals a regular one-dimensional stacking along the a axis (Figure S3 in the Supporting Information), which shows close $S2\cdots S3 = 3.571(1) \text{ \AA}$ contacts. Once again this differs from the crystal packing of **L**¹ for which a strong dimerisation was observed.^[17]

$[(L^2)Ln(hfac)_3]$ [$Ln = Y^{III}$ (4**), Er^{III} (**5**) and Yb^{III} (**6**)]**

These three compounds are isostructural. Therefore, the structure of **6** is described and the respective values for **4** and **5** are given in square brackets, respectively. Compound **6** [**4**, **5**] crystallises in the monoclinic $P2_1/c$ (no. 14) space group (Table 5). Compound **6** [**4**, **5**] is similar to **3** [**1**, **2**] with the asymmetric unit composed of one **L**² ligand and one $Yb(hfac)_3$ [$Y(hfac)_3$, $Er(hfac)_3$] unit (Figure 4) [Figures S4 and S5 in the Supporting Information], except that the hydrogen atom on N3 is replaced by a methyl-2-pyridine arm by alkylation. This arm is not coordinated to the lanthanide that remains linked to the (2-pyridyl)benzimidazole acceptor. The presence of this arm leads to significant structural modifications. In particular, a new arrangement of the $hfac^-$ anions is observed due to steric hindrance of the methyl-2-pyridine moiety. The coordination polyhedra preserve the D_{2d} symmetry but are now closer to the D_{4d} symmetry instead of C_{2v} (Table 2).

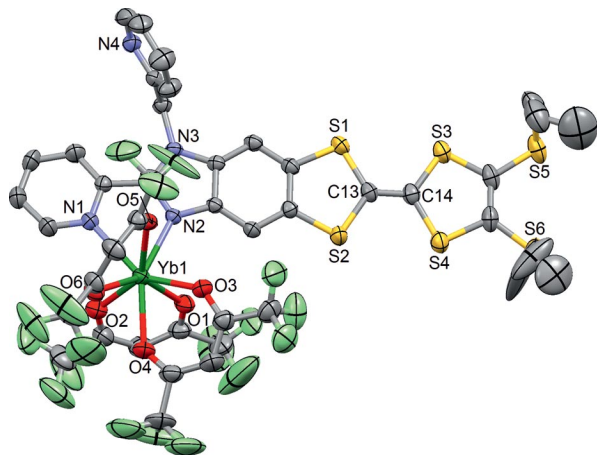


Figure 4. ORTEP view of the asymmetric unit of **6**. Thermal ellipsoids are drawn at 30% probability. Hydrogen atoms are omitted for clarity.

The crystal packing is also affected by the alkylation. Indeed the intermolecular A–A interactions are cancelled since no hydrogen-bond is present anymore. Only the intermolecular D–A interactions remain, and as a consequence the organic network is now composed of isolated dimers (Figure 2, b).

Electrochemical Properties

The electrochemical properties of the ligands and complexes were studied by cyclic voltammetry (Figure S6 in the

Supporting Information). For all samples, two reversible single-electron oxidation waves are observed that correspond successively to the formation of the radical cation and dicationic species (Table 3).

Table 3. Oxidation potentials (V versus SCE, nBu_4NPF_6 , 0.1 M in CH_2Cl_2 at 100 mV s^{-1}) of the ligands **L**¹ and **L**² and complexes **1**–**6**.

	$E_{1/2}^1$	$E_{1/2}^2$
L ¹	0.498	0.902
L ²	0.504	0.912
1	0.497	0.947
2	0.490	0.912
3	0.498	0.910
4	0.516	0.912
5	0.505	0.908
6	0.498	0.904

These values are anodically shifted relative to the oxidation potentials measured for the parent TTF (380 and 770 mV) due to the electron-withdrawing nature of the 2-pyridylbenzimidazole/2-pyridyl-1-(2-pyridylmethyl)benzimidazole substituents, which makes oxidation of the TTF core more difficult for the free ligands and coordination complexes. The evolution of the oxidation potentials between both ligands and after coordination of the trivalent lanthanides is very weak. The electrochemical properties attest to the reversibility of the oxidation.

Magnetic Properties: Er^{III} -Based Compounds **2** and **5**

The $\chi_M T$ versus T curves for compounds **2** and **5** are presented in Figure S7 of the Supporting Information. At room temperature, the $\chi_M T$ values (11.42 and $11.06 \text{ cm}^3 \text{ K mol}^{-1}$ for **2** and **5**, respectively) are close to the expected value for one isolated Er^{III} ion ($11.48 \text{ cm}^3 \text{ K mol}^{-1}$) with a $^4I_{15/2}$ multiplet ground state and $g_J = 6/5$.^[19] The $\chi_M T(T)$ curves decrease on cooling to reach values of 5.53 and $7.37 \text{ cm}^3 \text{ K mol}^{-1}$ at 2 K for **2** and **5**, respectively. The decrease follows the depopulation of the ligand-field levels that are constituted of linear combinations of M_J components of the total kinetic moment depending on the site symmetry.^[19]

Yb^{III} -Based Compounds **3** and **6**

The $\chi_M T$ versus T curves for compounds **3** and **6** are presented in Figure 5. At room temperature, the $\chi_M T$ values are rigorously identical for **3** and **6** ($2.315 \text{ cm}^3 \text{ K mol}^{-1}$) and close to the expected value for one isolated Yb^{III} ion ($2.57 \text{ cm}^3 \text{ K mol}^{-1}$) with an $^2F_{7/2}$ multiplet ground state and $g_J = 8/7$.^[19] On cooling, $\chi_M T$ versus T curves almost superimpose with a decrease in the $\chi_M T$ products to $1.05 \text{ cm}^3 \text{ K mol}^{-1}$ at 2 K. This decrease is also attributed to the depopulation of the M_J states of the multiplet ground state. At 2 K, the field dependence of the magnetisation differs significantly between **3** and **6** (Figure 5). Under 50 kOe, the magnetisation is equal to 1.6 and $1.47 N\beta$ for **3** and **6**, respectively. In the equivalent operators model, the crystal-field effect, which describes the zero-field splitting, is ex-

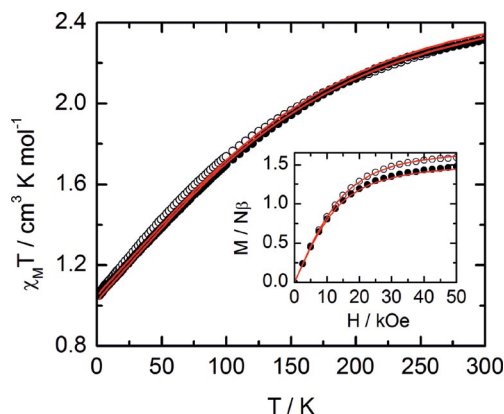


Figure 5. Thermal variation of the $\chi_M T$ products for **3** (black open circles) and **6** (black filled circles) with best-fit curves (red line). Inset: Magnetisation at 2 K for **3** (black open circles) and **6** (black filled circles) with the simulated curves (red lines).

pressed as polynomials of the total angular momentum matrices (J^2 , J_z , J_+ and J_-) in O_k^q operators.^[20,21]

$$H = \sum_{k=2,4,6} \sum_{q=-k}^k B_k^q O_k^q$$

M_J states are good quantum numbers of O_k^0 ($k = 2, 4, 6$), whereas a mixing occurs for $q \neq 0$. To reduce the number of free parameters it is necessary to consider higher symmetry than the real one. The coordination polyhedron in **3** is much more distorted than in **6** on account of the presence of the intermolecular hydrogen bond (Table 2). Indeed, in **6**, the polyhedron is almost as close to D_{2d} as D_{4d} , whereas in **3** the difference is much more pronounced. Then we considered a different symmetry for **3** and **6**: D_{2d} in **3** and D_{4d} in **6**. In the D_{2d} environment, the O_4^4 and O_6^6 operators must be added to the three O_k^0 that operate in D_{4d} environment.^[22] The best-fit curve for compound **6** is represented in Figure 5 (Table S1 in the Supporting Information). For **3**, we decided a priori to use the B_k^q values found for compound **6** to account for the similarities of the N_2O_6 environment while keeping only two free parameters (B_4^4 and B_6^6 ; Table S1 in the Supporting Information and Figure 5). The fits are satisfying and for both compounds the field dependence of the magnetisation at 2 K is reproduced well (Figure 5). It must be mentioned that for **3** it is impossible to

Table 4. Energy levels and eigenstates for compounds **3** and **6** extracted from the magnetic data (first two columns). The ground state is set at the origin. The last column contains the position in energy of the emission lines of the $^2F_{5/2} \rightarrow ^2F_{7/2}$ excitation with the most energetic line taken at the origin.

	Energy [cm ⁻¹]	Eigenstate	Emission
3	0	$0.976 \pm 5/2\rangle + 0.218 \pm 3/2\rangle$	0
	259	$0.976 \pm 3/2\rangle + 0.218 \pm 5/2\rangle$	234
	416	$0.973 \pm 7/2\rangle + 0.232 \pm 1/2\rangle$	409
	522	$0.973 \pm 1/2\rangle + 0.232 \pm 7/2\rangle$	504
6	0	$ \pm 5/2\rangle$	0
	251	$ \pm 3/2\rangle$	284
	459	$ \pm 7/2\rangle$	448
	544	$ \pm 1/2\rangle$	533

correctly reproduce the M versus H curve if considering a D_{4d} environment, which is a signature of the distortion of the coordination polyhedron.

In **6** the eigenstates are pure with an $M_J = \pm 5/2$ ground state, whereas of course in **3** the M_J states are mixed with a ratio 95:5% between $\pm 5/2$ and $\pm 3/2$ M_J states. The energy levels and the eigenstates are gathered in Table 4. As expected, the main contributions to the eigenvectors belong to the same M_J states in both compounds.

Photophysical Properties

Absorption Properties

The absorption properties of solutions of the free ligands **L¹** and **L²**, and complexes **1–6** in CH_2Cl_2 were studied (Figures 6 a, b, 7 a, b and Figure S9 in the Supporting Information). The Y^{III} -based compounds **3** and **6** were also studied in the solid state to allow comparisons of their emissive properties. To support and rationalise the experimental attributions of the absorption spectra, time-dependent density functional theory (TD-DFT) calculations were performed on the DFT-optimised geometries (see the Experimental Section) of the ligands **L¹** and **L²** and the Y^{III} analogues **1** and **4** (Figures 6 c, d, 7 c, d; Tables S1 and S2 in the Supporting Information). The absorption spectra of all the coordination complexes of the same series are identical and thus the experimental absorption spectrum of the Yb^{III} analogue can be compared with the Y^{III} calculated one. The corresponding molecular orbital (MO) diagrams are given in Figure S8 of the Supporting Information.

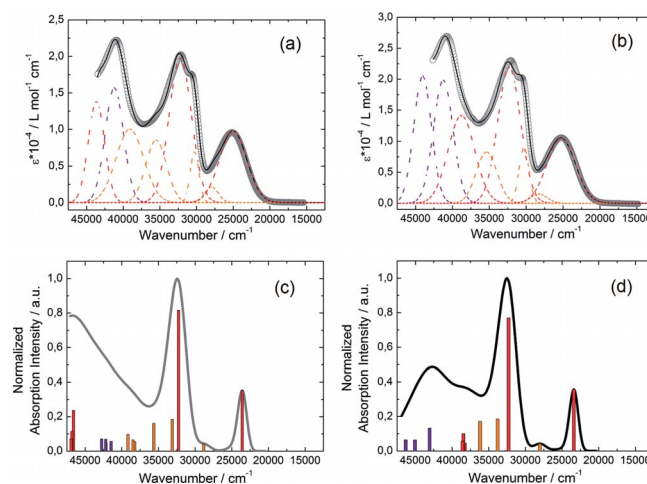


Figure 6. Experimental UV/Vis absorption spectra of solutions ($c = 4 \times 10^{-5}$ M) of ligands (a) **L¹** and (b) **L²** (open grey circles) in CH_2Cl_2 . Respective Gaussian decompositions (dashed lines) and best fit (full black line), $R = 0.9982$ for **L¹** and $R = 0.9992$ for **L²**. Theoretical absorption spectra of (c) **L¹** (grey line) and (d) **L²** (black line). The sticks represent the mean contributions of the absorption spectra that are listed in Table S1 in the Supporting Information.

The experimental absorption curve of **L¹** was deconvoluted into eight bands (Figure 6, a). The calculated UV/Vis absorption spectrum for **L¹** (Figure 6, c) reproduces the ex-

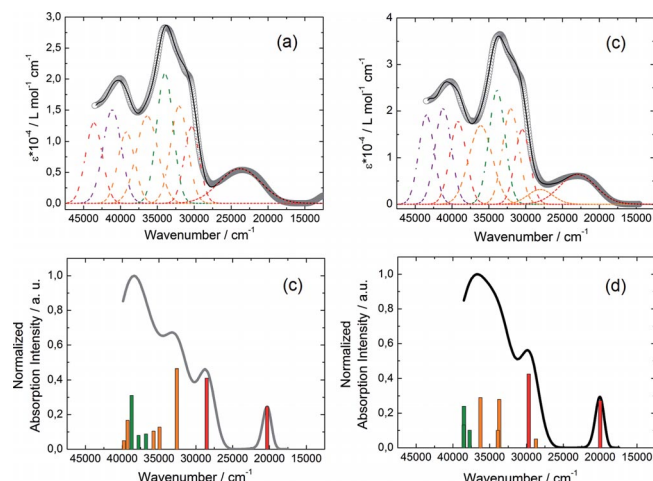


Figure 7. Experimental UV/Vis absorption spectra of solutions ($c = 4 \times 10^{-5}$ M) of (a) **1** and (b) **4** (open grey circles) in CH_2Cl_2 . Respective Gaussian decompositions (dashed lines) and best fit (full black line), $R = 0.9987$ for **1** and $R = 0.9990$ for **4**. Theoretical absorption spectra of (c) **1** (grey line) and (d) **4** (black line). The sticks represent the mean contributions of the absorption spectra that are listed in Table S3 in the Supporting Information.

perimental curve well. The low-energy band was calculated at the average value of 23582 cm^{-1} (experimental value at 25000 cm^{-1} , red Gaussian component) and attributed to $\pi-\pi^*$ HOMO \rightarrow LUMO TTF-to-ImPy intraligand charge transfers (ILCT) (Figure 6, Table S2 in the Supporting Information). The following five absorption bands centred at 27900 , 30300 , 32200 , 35500 and 39100 cm^{-1} were calculated at the average energies of 28843 , 33133 , 32270 , 35629 and 38623 cm^{-1} , respectively. They are all attributed to $\pi-\pi^*$ and $\pi-\sigma^*$ intra-TTF transitions (ID) except the strong one centred at 32200 cm^{-1} , which is attributed to the HOMO-1 \rightarrow LUMO (84%) ILCT (Table S1 in the Supporting Information). It is worth noting that for both ligands the calculations first give the HOMO-1 \rightarrow LUMO (84%) ILCT followed by the HOMO \rightarrow LUMO+4 (33%) ID on the energy scale, whereas the order is experimentally reversed. This is due to the underestimation of the energy of ILCT-type transitions in strongly conjugated systems. The highest-energy bands (41200 and 43700 cm^{-1} for the purple and red decompositions, respectively; Figure 6, a) are calculated at the average energies of 41945 and 46775 cm^{-1} , respectively. They are mainly attributed to intraligand (IL) and ILCT excitations. The experimental and calculated absorption properties of **L**² are similar to those of **L**¹. Nevertheless, the alkylation of the imidazole ring slightly increases the acceptor character of the coordinating moiety as attested by the calculated energies of the two strong HOMO \rightarrow LUMO (96%) (23401 cm^{-1}) and HOMO-1 \rightarrow LUMO (79%) (32300 cm^{-1}) ILCTs, which are lower in **L**² than in **L**¹. The calculations highlight the ILCT contributions that involve the HOMO+3 orbital centred on the methyl-2-pyridine unit in the excitations localised at 28038 and 38586 cm^{-1} .

TD-DFT calculations for the **Y**^{III} complexes were performed only in the 0 – 39500 cm^{-1} energy range (50 excitations) due to the size of the system to evaluate the coordi-

nation effect of the **Y**(hfac)₃ moiety. For **1**, the calculated data reproduce the experimental absorption curve well (Figure 7).

The lowest-energy bands were calculated at the average values of 20324 cm^{-1} (experimental value is found at 23800 cm^{-1} , red component) and are attributed to the $\pi-\pi^*$ HOMO \rightarrow LUMO (98%) ILCT. That is significantly lower (by 3258 cm^{-1}) than the energy calculated for the free ligand **L**¹ (23582 cm^{-1}) due to the electron-withdrawing effect of the **Y**(hfac)₃ moiety, which decreases the electron density of both acceptor- and donor-centred orbitals (Figure S8 in the Supporting Information). Thus, the LUMO and HOMO orbitals are stabilised by 5160 and 1370 cm^{-1} , respectively. The same reason explains the stabilisation (3733 cm^{-1}) of the HOMO-1 \rightarrow LUMO (98%) ILCT. The appearance of a new absorption band centred at 37764 cm^{-1} (experimental green component centred at 34000 cm^{-1}) is observed after coordination of the **Y**(hfac)₃ moiety. It is attributed to intra-hfac⁻ excitations. In a first approximation, the absorption properties of **4** are very similar to those of **1**. Nevertheless some differences are identified. The decrease in the electron density of the PyImPy acceptor due to the coordination of the **Y**(hfac)₃ moiety is slightly weaker than for the ImPy acceptor because the methyl-2-pyridine is not affected by this coordination. Thus, the slightly weaker stabilisation of the LUMO orbital after coordination (4676 cm^{-1}) leads to a mixing with the hfac⁻-centred orbitals (Figure S8 in the Supporting Information). Consequently, the LUMO and LUMO+1 orbitals are delocalised on the hfac⁻ anions and the PyImPy acceptor.

The absorption properties of **3** and **6** in the solid state give similar results to those in solution, except for the lowest-energy range in which an additional absorption band is observed (Figure S10 in the Supporting Information) that might be attributed to possible intermolecular charge transfers in solid-state.^[12b]

Emission Properties

Ligand-Centred Luminescence

The emission spectra of the ligands and related **Y**^{III} complexes are represented in Figure 8 and Figures S11–S13 in the Supporting Information. At room temperature, excitation at 26320 cm^{-1} (380 nm) in the $\pi-\pi^*$ HOMO \rightarrow LUMO ILCT (see above) of ligand **L**¹ results in a weak broad ligand-centred emission with a maximum at 19270 cm^{-1} (Figure S12 in the Supporting Information). For **L**², no fluorescence was observed under the same conditions. At 77 K , this emission disappears and an intense, structured signal appears with maxima at 17036 and 17065 cm^{-1} for **L**¹ (Figure S12 in the Supporting Information) and **L**² (Figure S13 in the Supporting Information), respectively. For the related **Y**^{III} derivatives **1** and **4**, a visible excitation of 21740 cm^{-1} (460 nm) was used to irradiate the $\pi-\pi^*$ HOMO \rightarrow LUMO ILCT. At room temperature, both complexes display a very weak ligand-centred fluorescence with maxima at 18597 and 18553 cm^{-1}

for **1** (Figure S14 in the Supporting Information) and **4** (Figure 8, a), respectively. For **1**, the stabilisation of 673 cm^{-1} of the $^1\pi\pi^*$ state with respect to L^1 is attributed to the coordination of the $Y(hfac)_3$ moiety. As for the free ligand, the decrease in the temperature to 77 K leads to the disappearance of the fluorescence, which aids the appearance of the almost identically structured signal observed for the free ligand with maxima at 17035 and 17095 cm^{-1} for **1** (Figure S14 in the Supporting Information) and **4** (Figure 8, a), respectively. The luminescence decay can be nicely fitted by a monoexponential function (Figure 8, b), thereby allowing the estimation of a very long lifetime (3.10 ms) for complex **4**. This result clearly confirms that the low-temperature structure emission corresponds to phosphorescence that arises from the ligand-centred triplet state.

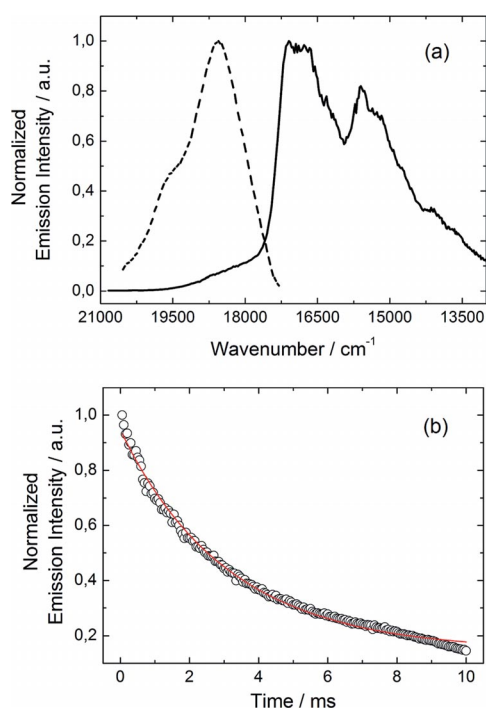


Figure 8. (a) Fluorescence spectrum at room temperature (dashed line) and phosphorescence spectrum (full line) at 77 K of **4** in the visible range for $\lambda_{\text{ex}} = 21740\text{ cm}^{-1}$ (460 nm) in CH_2Cl_2 . Spectra are normalised and not drawn on the same vertical scale. (b) Phosphorescence decay of **4** recorded at 16665 cm^{-1} (600 nm) in degassed CH_2Cl_2 at 77 K under 21740 cm^{-1} (460 nm) excitation for **4**. The red line represents monoexponential fit.

Metal-Centred Luminescence

Er^{III}-Based Complexes

Emission properties of solutions of **2** and **5** in CH_2Cl_2 were measured at 77 K and room temperature (Figure 9 and Figure S14 in the Supporting Information).

Upon irradiation at 21740 cm^{-1} in the lowest-energy absorption band ($\pi\text{-}\pi^*$ HOMO \rightarrow LUMO ILCT), two different emissions were observed and assigned to the ligand-centred phosphorescence at 16779 (for **2**) and 16835 cm^{-1} (for **5**), and to an emission centred at 6520 cm^{-1} (1534 nm)

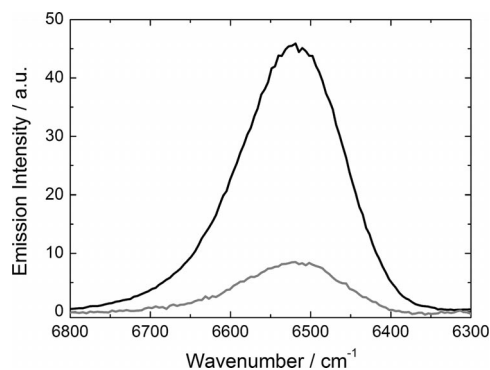


Figure 9. Luminescence spectra of **2** (grey line) and **5** (black line) in the NIR range for $\lambda_{\text{ex}} = 21740\text{ cm}^{-1}$ (460 nm) at 77 K in CH_2Cl_2 .

that is characteristic of the $\text{Er}^{\text{III}}\ 4\text{I}_{13/2} \rightarrow 4\text{I}_{15/2}$ transition. Increasing the temperature induces a broadening and a significant decrease in the metal-centred signal probably due to thermal vibrations, which favour nonradiative de-excitations. Nevertheless, the maxima of the luminescence signal remain at the same value. At room temperature, no ligand-centred emission is further observed. It was recently demonstrated that the presence of a low-energy ILCT transition can suggest a sensitisation that occurs directly through the transfer of energy from the charge-transfer state.^[12] The presence of the phosphorescence signal at 77 K suggests that the $^3\pi\pi^*$ state should be also involved in the sensitisation mechanism. In the present case, it is difficult to discriminate between the possible sensitisation processes, and both energy transfers from singlet and triplet excited states might occur simultaneously.

Yb^{III}-Based Complexes

Emission properties of **3** and **6** were studied at room temperature and 77 K in the solid state and in CH_2Cl_2 solution (Figure 10 and Figure S15 in the Supporting Information). The excitation of the samples with an energy of 21740 cm^{-1} induces an Yb^{III} ion-centred luminescence, which is assigned to the $^2\text{F}_{5/2} \rightarrow ^2\text{F}_{7/2}$ emission.

It is worth noting that the presence of low-energy ILCT transitions allows the sensitisation of Yb^{III} with long wavelength up to 530 nm localised in the visible part of the spectra. The energy of the donor excited state can be estimated from the zero-phonon transition wavelength $E_{0-0}(^1\pi\pi^*)$ at 20790 cm^{-1} for **3** (2.58 eV) and 20430 cm^{-1} for **6** (2.53 eV). As for Er^{III} analogues, sensitisation might occur through energy transfer from singlet and/or triplet excited states. In the particular case of Yb^{III} , an additional sensitisation process must be taken into account that involves a stepwise photoinduced electron transfer (ΔG_{ET}) in the case of electroactive ligands.^[23–25] It involves the transient formation of an oxidised donor/ Yb^{II} species and its feasibility can be estimated using the extended Rehm–Weller^[26] equation [Equation (1)]

$$\Delta G_{\text{ET}} \geq e_0(E_{\text{ox}} - E_{\text{red}}) - E_{0-0} - w \quad (1)$$

in which e_0 represents the elementary electron charge, E_{ox} the oxidation potential of the electro-donating ligand

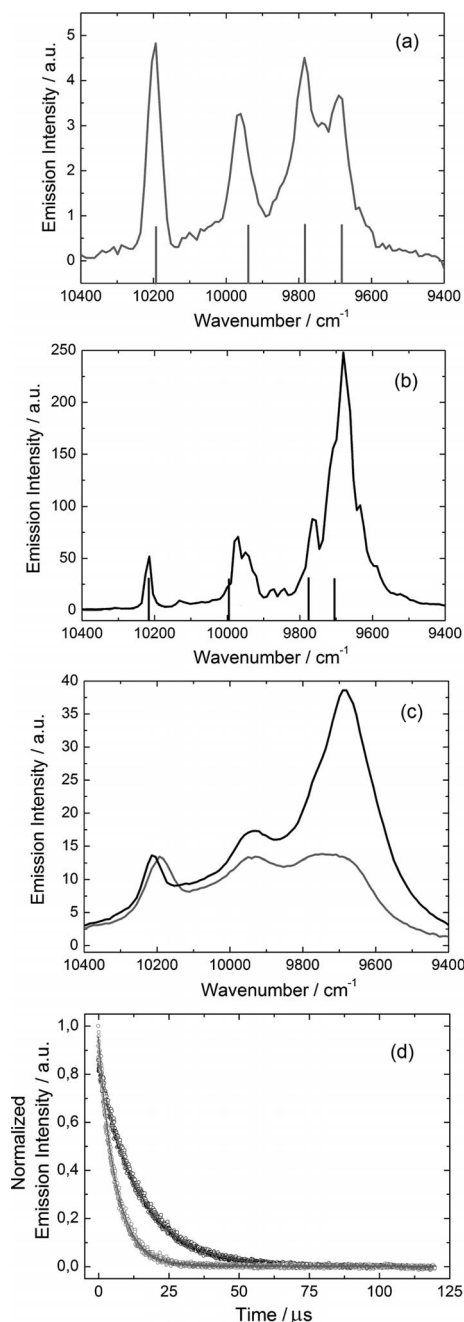


Figure 10. Luminescence spectra of (a) **3** (grey line) with the calculated energy splitting (vertical grey sticks) and (b) **6** (black line) with the calculated energy splitting (vertical black sticks) in the NIR range for $\lambda_{\text{ex}} = 21740 \text{ cm}^{-1}$ (460 nm) in the solid state at 77 K. (c) Luminescence spectra of **3** (grey line) and **6** (black line) in the NIR range for $\lambda_{\text{ex}} = 21740 \text{ cm}^{-1}$ (460 nm) in the solid state at room temperature. (d) Decay kinetics of $^2\text{F}_{5/2}$ recorded at 10200 cm^{-1} (980 nm) in degassed CH_2Cl_2 at room temperature under 21740 cm^{-1} (460 nm) excitation for **3** (open grey circles) and **6** (open black circles). The red lines represent monoexponential fits.

(0.498 V versus SCE), E_{red} the reduction potential of the Yb^{III} ion (−1.65 V versus SCE) and E_{0-0} the excited-state energy (2.58 and 2.53 eV for **3** and **6**, respectively). In addition, w represents the stabilisation energy between the different components of the ion pair (0.15 eV for a closely as-

sociated ion pair). Thus, ΔG_{ET} values are equal to −0.582 and −0.577 V for **3** and **6**, respectively. One can note that by taking into account the triplet state instead of the singlet one, the ΔG_{ET} values remain negative, which suggests that the electron-transfer process might be thermodynamically favoured. In other words, the Yb^{III} luminescence sensitisation mechanism could involve a photoinduced electron transfer (PET).

At room temperature in CH_2Cl_2 , the luminescence decay corresponds to a single exponential function of the time that is synonymous with a $^2\text{F}_{5/2}$ state lifetime of 6.2 and 14.6 μs for complexes **3** and **6**, respectively (Figure 10, d). Such decay lifetimes are in the range of the standard $\{\text{Yb}(\text{hfac})_3(\text{diimine})\}$ luminophores.^[22,27c] The longer lifetime observed for **6** than **3** can be attributed to the alkylation of the imidazole ring in **6** that cancels out the N–H oscillators. In fact, the alkylation, halogenation or deuteration are well-known synthetic routes to reduce the oscillations and increase the efficiency of the luminescence.^[28] The effect of the alkylation on the efficiency of the NIR luminescence is also qualitatively visible by comparing the intensity of the emission. Complexes **5** and **6** clearly display a more intense NIR luminescence than the corresponding nonalkylated complexes **2** and **3** (Figure 9 and Figure 10). In the solid state at 77 K, an identical excitation leads to a more structured signal (Figure 10a and b). The comparison of the shapes of the spectra in solution and in the solid state reveals some differences that should be attributed to a reorganisation of the hfac^- anions in solution.^[29] At low temperature, for **3**, four transitions are clearly identified at 10194, 9960, 9785 and 9690 cm^{-1} that correspond to the degeneracy of the $^2\text{F}_{7/2}$ ground state (Kramer's doublets). One more transition could be identified at 9737 cm^{-1} and it might be due to the participation of an excited M_J state of the $^2\text{F}_{5/2}$ multiplet. For **6**, the previous four components were identified at 10214, 9930, 9766 and 9681 cm^{-1} , but at least two additional contributions are present at 9970 and 9715 cm^{-1} . These new contributions could be due to the $^2\text{F}_{5/2} \rightarrow ^2\text{F}_{7/2}$ excitation that arises from the second M_J state of the excited $^2\text{F}_{5/2}$ level ($\Delta E = 40 \text{ cm}^{-1}$). The total splitting of the ground state was determined to be equal to 504 (for **3**) and 533 cm^{-1} (for **6**) from the various crystal-field sublevels identified at 77 K.

These values can be compared with the splitting previously observed for Yb^{III} ion in a distorted (455 cm^{-1}) and regular (372 cm^{-1}) D_3 symmetry, whereas a splitting of 528 cm^{-1} was found for Yb^{III} complexes in low symmetry.^[30] The present values thus correspond to low symmetry, which is in agreement with the distorted triangular dodecahedron polyhedra around the Yb^{III} ion in **3** and **6** (see above).

Ab Initio Calculations

To gain more insight into the magnetic and luminescent properties of Yb^{III} complexes **3** and **6**, CASSCF/RASSI-SO calculations were carried out on molecular models based on

the X-ray crystal structures (see the Experimental Section). Indeed, to properly account for the competition between the spin–orbit coupling, crystal-field interactions and the multiconfigurational nature of the wavefunction in lanthanide-based compounds, explicitly correlated *ab initio* methods are required. Such an approach was already successfully applied for numerous monometallic Dy^{III} SMMs,^[15a,31] whereas examples of its use for Yb^{III} complexes are still scarce.^[15b,32] First, we concentrated on complex **6** to calibrate our calculation procedure with respect to the energy splitting extracted from the luminescent experiments. At the CASSCF level, the splitting of the ground-state multiplet is strongly underestimated, which is no longer the case if MS-CASPT2 corrections are applied on top of the spin-free wavefunction (see Table S4 and Figure S16 in the Supporting Information). At this level of calculation, an excellent agreement with the experimental energy splitting is obtained (i.e. 0, 210, 436 and 503 cm^{−1} versus 0, 284, 448 and 533 cm^{−1}; see Figure 10, b). This gives us confidence in using the computed data in the interpretation of the magnetic properties. The g_z value calculated for the ground-state doublet ($g_z = 5.3$; Table S4 in the Supporting Information) is compatible with the expected value ($g_z = 5.71$) for a pure $M_J = 5/2$ ground state in the effective spin $1/2$ model. The calculated energy splitting and the nature of the M_J ground state are in accordance with the experimental magnetic data since both thermal variation of the $\chi_M T$ product and the magnetisation at 2 K are reproduced well (Figure S17 in the Supporting Information). The calculated anisotropy direction lies in the less electronegative orientation (i.e., principally along the nitrogen atoms of the imidazole–pyridine acceptor) (Figure 11).

A similar procedure was then undertaken for **3** with again a perfect match between MS-CASPT2 relative energy splitting (0, 252, 407, 504 cm^{−1}) and luminescence data (0, 234, 409, 504 cm^{−1}) (Figure 10a, Figure S16 and Table S4 in the Supporting Information). However, as shown by (1) the calculated g_z value ($g_z = 6.7$; Table S4 in the Supporting Information) that strongly differs from the expected $g_z = 5.71$ for a pure $M_J = 5/2$ ground state and (2) the computed magnetic susceptibility and magnetisation curves that do not reproduce the experimental results (Figure S17 in the Supporting Information), the calculated data on the molecular model of **3** do not allow a correct description of the ground state. At first, this result appeared surprising since our approach does work correctly for **6**, and complexes **3** and **6** can be considered close cousins. Among the main structural differences between these two Yb^{III} compounds, a hydrogen bond between the protonated imidazole ring and the oxygen atom of the neighbouring molecule was evidenced in **3**, whereas the presence of the methyl-2-pyridine arm prevents such weak interactions between neighbouring molecules in **6**. To investigate the effect of this hydrogen bond on the spectroscopic properties of **3**, the neighbouring complex was modelled by an imidazole molecule (Figure S19 in the Supporting Information). The hydrogen atom involved in the hydrogen bond was then described with an extended [3s2p1d] basis set to catch as much as

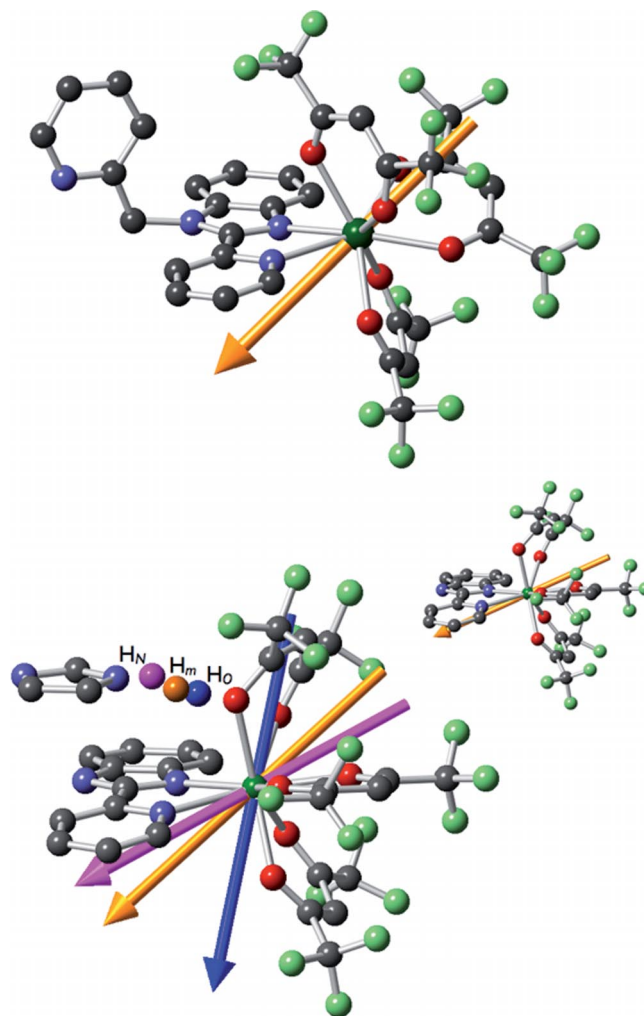


Figure 11. Orientation of the ground-state anisotropy axis for **3** (bottom) and **6** (top). For **3**, the orientation of the axis is given for the different positions of the hydrogen atom involved in the hydrogen bond (H_O in blue, H_m in yellow and H_N in purple) and without the imidazole moiety (in inset).

possible the electronic reorganisation that might be induced by this weak interaction. Another critical aspect concerns the position of the H atom. We thus arbitrarily decided to localise it (1) at the position calculated from X-rays (H_N), (2) along the O...N axis at a classical O–H distance (H_O) and (3) at the equidistance of N and O (H_m). On the one hand, the presence of this hydrogen bond in the calculation only slightly affects the relative energy splitting of the ground-state multiplet (Table S4 in the Supporting Information). Only with H_O is this splitting reduced with a first excited state much closer to the ground state. On the other hand, the effect on the magnetic properties is clearly demonstrated with a g_z value that decreases in the order $H_N > H_m > H_O$ (Table S4 in the Supporting Information). At the last position, $g_z = 5.8$ becomes close enough to the critical $g_z = 5.71$ to envision a majority of $M_J = 5/2$ in the ground-state wavefunction.

Concomitantly, the magnetic susceptibility and magnetisation curves are progressively closer to the experimental

ones (Figure S17 in the Supporting Information). The effect on the ground-state magnetic axis is also non-negligible since its orientation clearly depends on the position of the proton (i.e., the magnetic axis progressively rotates in the direction of the proton when the position of the latter progressively moves closer to the lanthanide ion) (Figure 11). It is worth noting that an inverse behaviour was observed in a Dy^{III} mononuclear complex,^[15a] which is in agreement with the prolate Yb^{III} electronic distribution relative to the oblate Dy^{III} one. Even if a perfect agreement with the experimental results is not fulfilled with this computational description, it does, however, strongly suggest the prominent role of hydrogen bonds and, in consequence, of crystal structure engineering in the design of future molecular magnets.

Correlation between Luminescence and Magnetic Properties

On the one hand, magnetisation measurements when varying the temperature provide an indirect photograph of the ground-state multiplet splitting through Boltzmann population of the crystal-field levels. On the other hand, light emission toward the ground-state multiplet gives a direct image of the crystal-field effects. Then these two different techniques were used to probe the same energy levels and can thus be assessed.^[14,15,33]

In this line, the emission spectra at 77 K of **3** and **6** were directly compared with the energy levels extracted from the magnetic measurements (Figure 12). These energy levels and the corresponding eigenstates calculated from the fitting of the magnetic data of compounds **3** and **6** are given in Table 4. Since in the Russell–Saunders coupling scheme the emission spectrum acts as a photograph of the multiplet ground-state splitting, the energy position of the emission lines of the $^2F_{5/2} \rightarrow ^2F_{7/2}$ excitations relative to the most

energetic line were also added in Table 4. For both compounds **3** and **6**, the luminescence peak positions are fairly well reproduced with the data extracted from magnetism. Therefore the emission lines can be unambiguously attributed and the energy-level splitting of the ground-state multiplet $^2F_{7/2}$ that results from the crystal effects identified as a linear combination of M_J states.

Inversely, the correlation luminescence versus magnetism might emerge from the regeneration of the magnetic data using the luminescence information as input. Let us focus on the D_{4d} symmetry that was considered for compound **6** (see above). In this symmetry, the energy levels in the ground-state multiplet $^2F_{7/2}$ can be calculated as a function of the three parameters B_2^0 , B_4^0 and B_6^0 and the energy gaps between these levels expressed relatively to the ground state. From the four luminescence peak positions at 0, 284, 448 and 533 cm⁻¹, three energy gaps are accessible, thereby making it possible to solve a set of equations with three unknown parameters. However, since the eigenstates are not known a priori, 24 possible arrangements of the M_J states in the four levels might be considered (Table S5 in the Supporting Information). Thus, for each arrangement, the temperature dependence of the magnetic susceptibility was calculated and compared to the experimental results (Figure S18 in the Supporting Information). The arrangements with the ground state $\pm 7/2$, $\pm 3/2$ or $\pm 1/2$ can be excluded since they generate a low-temperature limit of $\chi_M T$ equal to 2.00, 0.38 and 1.35 cm³ K mol⁻¹, respectively. The closest simulation is obtained with an energy-level sequence of $M_J = \pm 5/2$ (0 cm⁻¹), $\pm 3/2$ (284 cm⁻¹), $\pm 7/2$ (448 cm⁻¹) and $\pm 1/2$ (533 cm⁻¹), which closely coincides with the sequence previously extracted from the fitting of the $\chi_M T$ versus T curve (Figure S17 in the Supporting Information) with nearly identical Stevens parameters $B_2^0 = -1.51$ cm⁻¹, $B_4^0 = 0.384$ cm⁻¹ and $B_6^0 = 1.038 \times 10^{-3}$ cm⁻¹.

Conclusion

Two families of mononuclear complexes of the formula [Ln(hfac)₃(L¹)] and [Ln(hfac)₃(L²)] with Ln^{III} = Y, Er and Yb were synthesised and crystallised. Ligand L¹ consists of a TTF core functionalised by the 2-pyridylbenzimidazole acceptor, whereas L² is the 2-methylpyridine alkylated form of L¹. The alkylation of L¹ leads to significant distortion of the coordination polyhedron. These structural changes directly affect the magnetic and photophysical properties.

For the Yb^{III} derivatives, the thermal dependence of the $\chi_M T$ products were fitted and the energy splitting of the M_J energy states of the $^2F_{7/2}$ multiplet ground state was determined. Ab initio calculations clearly demonstrate the role of the imidazole proton in the energy splitting and the nature of the M_J ground state and explain why the alkylation affects the energies and the nature of these M_J levels. In fact, the anisotropy axis of the ground state lies in the less electronegative direction in agreement with the prolate Yb^{III} ion.

Irradiation at 21740 cm⁻¹ of the Y^{III} derivatives led to weak fluorescence of the ligands at room temperature and

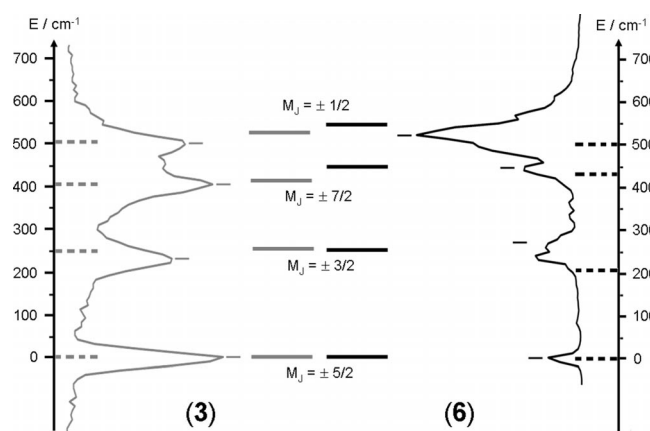


Figure 12. The solid-state 77 K emission spectra are represented with an appropriate shift of the energy scale. Diagram of energy levels for compounds **3** (grey lines) and **6** (black lines) calculated with the parameters given in main text from the magnetic measurements. Labels correspond to the M_J values. Diagram of energy levels for compounds **3** (dashed grey lines) and **6** (dashed black lines) obtained by MS-CASPT2/RASSI-SO calculations.

phosphorescence at 77 K. Under the same excitation, the Er^{III} and Yb^{III} derivatives displayed classical metal-centred luminescence, which is attributed to the $^4\text{I}_{13/2} \rightarrow ^4\text{I}_{15/2}$ and $^2\text{F}_{5/2} \rightarrow ^2\text{F}_{7/2}$ transitions, respectively. The alkylation led to (1) an enhancement of the lanthanide emission intensity due to the suppression of the N–H oscillator, (2) a substantial increase in the excited-state lifetime (from 6.2 to 14.6 μs) and (3) a change of the shape of the Yb^{III} -centred luminescence that is perfectly reproduced by ab initio calculations with MS-CASPT2 corrections.

This work clearly demonstrates that (1) the shape of the luminescent signal of lanthanides subtly depends on the crystal field (energy splitting of the M_J states) and (2) the luminescence and the magnetism can be experimentally and theoretically correlated, thus opening the door to subsequent investigations on the electronic effects at the root of these behaviours.

Next, we will exploit the prominent role of crystal structure engineering in the design of future molecular magnets to control the magnetic properties. Moreover, the Yb^{III} complexes presented herein might be good candidates for photoinduced conducting materials based on organic TTF derivatives and thus offer new attractive ways to achieve photoswitchable conducting materials that involve metal-centred luminescence.

Experimental Section

General: All solvents were dried using standard procedures. 5,6-Diamino-2-[4,5-bis(propylthio)-1,3-dithio-2-ylidene]benzo[d]-1,3-dithiole^[34] and $\text{Dy}(\text{hfac})_3 \cdot 2\text{H}_2\text{O}$ ^[35] were prepared according to literature procedures. All other reagents were purchased from Aldrich Co. Ltd and were used without further purification.

Synthesis of the Ligands L^1 and L^2 and Complexes 1–6

2-{4,5-[4,5-Bis(propylthio)tetrathiafulvalenyl]-1H-benzimidazol-2-yl}pyridine (L^1) and 4,5-Bis(propylthio)tetrathiafulvalene-2-(2-pyridyl)benzimidazole-methyl-2-pyridine (L^2): 2-Pyridinecarbaldehyde (1.5 equiv., 0.3 mL, 3 mmol) was slowly added to a solution of 5,6-diamino-2-[4,5-bis(propylthio)-1,3-dithio-2-ylidene]benzo[d]-1,3-dithiole (0.909 g, 2.1 mmol) in 1,4-dioxane and was stirred overnight under an aerobic atmosphere. The resulting solution was evaporated to dryness and the red oil was purified by silica flash chromatography (2:1 CH_2Cl_2 /ethyl acetate as eluant). The ligands were obtained as a pale orange powder for L^1 [Yield: 305 mg (28%)] and a bright orange powder for L^2 [yield: 244 mg (19%)]. The ^1H NMR and IR (KBr) measurements for L^1 give similar results to those previously published.^[16] For L^2 : ^1H NMR (CDCl_3): δ = 1.04 (t, 6 H), 1.73 (m, 4 H), 2.84 (t, 4 H), 4.13 (s, 2 H), 7.04 (m, 2 H), 7.21 (m, 2 H), 7.59 (m, 2 H), 7.74 (m, 1 H), 7.92 (m, 1 H), 8.61 (m, 2 H) ppm. IR (KBr): $\tilde{\nu}$ = 3428, 3261, 1625, 1597, 1444, 1417, 1392, 1090, 880, 788 cm^{-1} . Orange single crystals of L^2 were obtained by slow evaporation of a saturated solution of the ligand in CH_2Cl_2 .

$[(\text{L}^i)\text{Ln}(\text{hfac})_3]$ [$\text{Ln} = \text{Y}^{\text{III}}$ (1), Er^{III} (2) and Yb^{III} (3)]: A solution of L^1 (10.4 mg, 0.02 mmol) in CH_2Cl_2 and $\text{Ln}(\text{hfac})_3 \cdot 2\text{H}_2\text{O}$ (0.02 mmol) (14.9 mg for 1, 16.5 mg for 2 and 16.6 mg for 3) was stirred for 1 h. *n*-Hexane was layered into the solution, and red prismatic single crystals of 1, 2 and 3 were obtained after two weeks of diffusion and evaporation, yields: 15.5 (63%), 14.4 (55%) and

15.0 mg (57%) for 1, 2 and 3, respectively. $\text{C}_{37}\text{H}_{24}\text{F}_{18}\text{N}_3\text{O}_6\text{S}_6\text{Y}$ (1229.8): calcd. C 36.13, H 1.95, N 3.42; found C 36.09, H 2.02, N 3.39. $\text{C}_{37}\text{H}_{24}\text{ErF}_{18}\text{N}_3\text{O}_6\text{S}_6$ (1308.2): calcd. C 33.96, H 1.84, N 3.21; found C 34.05, H 1.90, N 3.22. $\text{C}_{37}\text{H}_{24}\text{F}_{18}\text{N}_3\text{O}_6\text{S}_6\text{Yb}$ (1313.9): calcd. C 33.82, H 1.83, N 3.20; found C 33.89, H 1.89, N 3.27.

$[(\text{L}^2)\text{Y}(\text{hfac})_3]$ [$\text{Ln} = \text{Y}^{\text{III}}$ (4), Er^{III} (5) and Yb^{III} (6)]: A solution of L^2 (12.2 mg, 0.02 mmol) in CH_2Cl_2 and $\text{Ln}(\text{hfac})_3 \cdot 2\text{H}_2\text{O}$ (0.02 mmol) (14.9 mg for 4, 16.5 mg for 5 and 16.6 mg for 6) was stirred for 1 h. Red prismatic single crystals of 4, 5 and 6 were obtained after two days of slow evaporation, yield 17.6 mg (63%). $\text{C}_{43}\text{H}_{29}\text{F}_{18}\text{N}_4\text{O}_6\text{S}_6\text{Y}$ (1320.9): calcd. C 37.03, H 2.08, N 4.02; found C 37.10, H 2.14, N 4.09. $\text{C}_{43}\text{H}_{29}\text{ErF}_{18}\text{N}_4\text{O}_6\text{S}_6$ (1399.3): calcd. C 37.03, H 2.08, N 4.02; found C 37.10, H 2.14, N 4.09. $\text{C}_{43}\text{H}_{29}\text{F}_{18}\text{N}_4\text{O}_6\text{S}_6\text{Yb}$ (1405.1): calcd. C 37.03, H 2.08, N 4.02; found C 37.10, H 2.14, N 4.09.

Crystallography: Single crystals were mounted on a Nonius four-circle diffractometer equipped with a CCD camera and a graphite-monochromated Mo- K_α radiation source (λ = 0.71073 Å), from the Centre de Diffractométrie (CDIFX), Université de Rennes 1, France. Data were collected at 293 K. Structures were solved with direct methods using the SIR-92 or SIR-97 programs and refined with a full-matrix least-squares method on F^2 using the SHELXL-97 program.^[36] Crystallographic data are summarised in Table 5.

CCDC-934920 (for 1), -934921 (for 2), -934922 (for 3), -934923 (for L^2), -934924 (for 4), -934925 (for 5) and -934926 (for 6) contain the supplementary crystallographic data for this paper. These data can be obtained free of charge from The Cambridge Crystallographic Data Centre via www.ccdc.cam.ac.uk/data_request/cif.

Physical Measurements: Elemental analysis of compounds 1–6 was performed at the Centre Régional de Mesures Physiques de l'Ouest, Rennes. Optical spectra were measured using the KBr disk method with a Perkin–Elmer 1600 Series FTIR instrument (resolution 4 cm^{-1}) for infrared (IR). ^1H NMR spectra were recorded with a Bruker Ascend 400 spectrometer. Chemical shifts are reported in parts per million referenced to TMS for ^1H NMR spectroscopy. Cyclic voltammetry was carried out in CH_2Cl_2 that contained 0.1 M $\text{N}(\text{C}_4\text{H}_9)_4\text{PF}_6$ as supporting electrolyte. Voltammograms were recorded at 100 mV s^{-1} with a platinum disk electrode. The potentials were measured versus a saturated calomel electrode (SCE). The luminescence spectra were measured with a Horiba–JobinYvon Fluorolog-3 spectrofluorimeter equipped with a three-slit double-grating excitation and emission monochromator with dispersions of 2.1 nm mm^{-1} (1200 grooves mm^{-1}). The steady-state luminescence was excited by unpolarised light from a 450 W xenon CW lamp and detected at an angle of 90° for diluted solution measurements or at 22.5° for solid-state measurements (front face detection) with a Peltier-cooled red-sensitive Hamamatsu R2658P photomultiplier tube (300–1010 nm). Spectra were reference-corrected for both the excitation-source light-intensity variation (lamp and grating) and the emission spectral response (detector and grating). Uncorrected near-infrared spectra were recorded at an angle of 45° with a liquid-nitrogen-cooled solid indium/gallium/arsenic detector (850–1600 nm). The excitation of the Yb^{III} luminescence decays was performed with an optical parametric oscillator from EKSPLA NT342 pumped with a pulsed-frequency-tripled YAG:Nd laser. The pulse duration was 6 ns at 10 Hz repetition rate. The detection was ensured with a R1767 Hamamatsu photomultiplier through a Jobin–Yvon monochromator equipped with a 1 μm blazed grating. The signal was visualised and averaged with a Lecroy digital oscilloscope LT342. The dc and ac magnetic-susceptibility measurements were performed on a solid polycrystalline sample with a Quantum Design MPMS-XL SQUID magnetometer between 2 and 300 K in an applied magnetic field of 0.2 T for temperatures

Table 5. X-ray crystallographic data for complexes **1–6** and ligand **L²**.

	[Y(hfac) ₃ (L ¹)] (1)	[Er(hfac) ₃ (L ¹)] (2)	[Yb(hfac) ₃ (L ¹)] (3)	L ²
Formula	C ₃₇ H ₂₄ YF ₁₈ N ₃ O ₆ S ₆	C ₃₇ H ₂₄ ErF ₁₈ N ₃ O ₆ S ₆	C ₃₇ H ₂₄ YbF ₁₈ N ₃ O ₆ S ₆	C ₂₈ H ₂₆ N ₄ S ₆
<i>M_r</i> [g mol ^{−1}]	1228.9	1308.3	1313.0	610.9
Crystal system	triclinic	triclinic	triclinic	triclinic
Space group	<i>P</i> $\bar{1}$ (no. 2)	<i>P</i> $\bar{1}$ (no. 2)	<i>P</i> $\bar{1}$ (no. 2)	<i>P</i> $\bar{1}$ (no. 2)
<i>a</i> [Å]	12.0845(3)	12.0838(5)	12.0883(4)	5.2845(4)
<i>b</i> [Å]	13.9962(5)	13.9925(6)	13.9875(4)	15.1248(12)
<i>c</i> [Å]	15.1282(5)	15.1161(5)	15.1028(3)	17.8565(14)
α [°]	101.040(2)	101.138(2)	101.286(2)	104.618(4)
β [°]	04.992(2)	105.033(2)	105.153(2)	94.021(4)
γ [°]	94.747(2)	94.770(2)	94.861(2)	91.796(4)
<i>V</i> [Å ³]	2402.17(13)	2397.84(16)	2392.16(12)	1375.84(19)
<i>Z</i>	2	2	2	2
<i>T</i> [K]	293 (2)	293 (2)	293 (2)	150(2)
Diffraction reflection	8.34 ≤ 2θ ≤ 55.06	2.86 ≤ 2θ ≤ 54.24	3.00 ≤ 2θ ≤ 60.96	2.36 ≤ 2θ ≤ 54.98
$\rho_{\text{calcd.}}$ [g cm ^{−3}]	1.699	1.812	1.823	1.475
μ [mm ^{−1}]	1.591	2.133	2.334	0.525
Number of reflections	19217	18200	22058	16835
Independent reflections	10975	10570	14445	6178
$R^2_{\text{o}} > 2\sigma(F_{\text{o}})^2$	6096	7133	9217	4106
Number of variables	650	635	696	343
<i>R</i> _{int} , <i>R</i> ₁ , <i>wR</i> ₂	0.0482, 0.0675, 0.1668	0.0420, 0.0562, 0.1441	0.0396, 0.0547, 0.1313	0.0559, 0.0544, 0.1572
	[Y(hfac) ₃ (L ²)] (4)	[Er(hfac) ₃ (L ²)] (5)	[Yb(hfac) ₃ (L ²)] (6)	
Formula	C ₄₃ H ₂₉ YF ₁₈ N ₄ O ₆ S ₆	C ₄₃ H ₂₉ ErF ₁₈ N ₄ O ₆ S ₆	C ₄₃ H ₂₉ YbF ₁₈ N ₄ O ₆ S ₆	
<i>M_r</i> [g mol ^{−1}]	1321.0	1399.3	1405.0	
Crystal system	monoclinic	monoclinic	monoclinic	
Space group	<i>P</i> 2 ₁ / <i>c</i> (no. 14)	<i>P</i> 2 ₁ / <i>c</i> (no. 14)	<i>P</i> 2 ₁ / <i>c</i> (no. 14)	
<i>a</i> [Å]	14.2288(3)	14.2026(3)	14.1771(4)	
<i>b</i> [Å]	21.3093(10)	21.2852(6)	21.2223(7)	
<i>c</i> [Å]	17.8700(7)	17.8394(3)	17.8268(6)	
β [°]	97.837(2)	97.7450(10)	97.520(2)	
<i>V</i> [Å ³]	5367.7(3)	5343.7(2)	5317.4(3)	
<i>Z</i>	4	4	4	
<i>T</i> [K]	293(2)	293(2)	293(2)	
Diffraction reflection	6.36 ≤ 2θ ≤ 51.34	2.90 ≤ 2θ ≤ 51.38	4.6 ≤ 2θ ≤ 52.20	
$\rho_{\text{calcd.}}$ [g cm ^{−3}]	1.635	1.728	1.755	
μ [mm ^{−1}]	1.431	1.916	2.107	
Number of reflections	16212	19330	18407	
Independent reflections	9852	10147	10494	
$R^2_{\text{o}} > 2\sigma(F_{\text{o}})^2$	6386	7045	7015	
No. of variables	713	780	787	
<i>R</i> _{int} , <i>R</i> ₁ , <i>wR</i> ₂	0.0362, 0.0639, 0.1610	0.0326, 0.0453, 0.1131	0.0306, 0.0495, 0.1231	

of 2–20 K and 1 T for temperatures of 20–300 K. The experimental data were corrected from the diamagnetism of the sample holder, and the intrinsic diamagnetism of the materials was evaluated with Pascal's table.

Computational Details: DFT geometry optimisations and TD-DFT excitation energy calculations of the ligands **L¹** and **L²**, and Y^{III} analogues (**1** and **4**) were carried out with the Gaussian 09 (revision A.02) package^[37] by employing the PBE0 hybrid functional.^[38] The "Stuttgart, Germany/Dresden" basis sets and effective core potentials were used to describe the yttrium atom,^[39] whereas all other atoms were described with the SVP basis sets.^[40] A similar strategy was already successfully used on similar complexes.^[41] The first 50 monoelectronic excitations were calculated for ligands **L¹**, **L²** and for complexes **1** and **4**. In all steps, a modelling of bulk solvent effects (solvent: CH₂Cl₂) was included through the polarisable continuum model (PCM)^[42] by using a linear-response non-equilibrium approach for the TD-DFT step.^[43] Molecular orbitals were sketched using the Gabedit graphical interface.^[44] Ab initio calculations were carried out for the Yb^{III} compounds **3** and **6** using the CASSCF/RASSI-SO/SINGLE_ANISO approach as implemented

in the MOLCAS 7.6 quantum chemistry package.^[45] In this approach, the relativistic effects are treated in two steps based on the Douglas–Kroll Hamiltonian. First, the scalar terms are included in the basis-set generation and are used to determine the spin-free wave functions and energies in the complete active space self-consistent field (CASSCF) method.^[46] Next, spin–orbit coupling was added within the restricted active space state interaction (RASSI-SO) method, which uses the spin-free wave functions as basis states.^[47] The resulting wave functions and energies are used to compute the magnetic properties, the free-ion parentages and the *g* tensors of the lowest states from the energy spectrum using the SINGLE-ANISO routine.^[48] Moreover, the effects of dynamic correlation were treated by means of multistate CASPT2 (MS-CASPT2) calculations on top of the spin-free wavefunctions. MS-CASPT2 calculations were restricted to the Ln atom and its first neighbours.^[49] For both systems, calculations were performed on a simplified version of the complex, where the donor part of the ligand was replaced by two H atoms (Figure S19 in the Supporting Information) since this part of the ligand was shown not to influence the magnetism of such systems in any way. To account for the hydrogen bond induced by the crystal packing of **3**, calculations

were also performed with an imidazole molecule that mimicked the position of the neighbouring molecule (Figure S19 in the Supporting Information). To account for the uncertainty in the position of the hydrogen atom of the hydrogen bond, this hydrogen atom was placed at three different positions along the O...N axis. All atoms were represented by ANO-type basis sets from the ANO-RCC library. The following contractions were used: [9s8p5d4f3g1h] for the Yb ion, [4s3p2d] for the O and the two most central N atoms (first coordination sphere around the Yb ion), [3s2p] for the C, F and remaining N atoms, [3s2p1d] for the H atom involved in the hydrogen bond and [2s] for all the other H atoms. The active space of the self-consistent field (CASSCF) method consisted of the thirteen 4f electrons of the Yb ion spanning the seven 4f orbitals. For a proper description of the spin-orbit coupling on the metal site, the mixing of a large number of states is required. In the present work, state-averaged CASSCF calculations were performed for all the doublets (seven roots) of the Yb ion, all of which were included in the RASSI-SO calculation. The anisotropy tensor of the ground spin-orbit state, as well as the temperature-dependent magnetic susceptibility, the molar magnetisation at 2 K and the energy spectrum were computed to support experimental results.

Supporting Information (see footnote on the first page of this article): Experimental details for physical characterisation and complete crystal structure results as a CIF file including bond lengths, angles, and atomic coordinates are deposited as Supporting Information.

Acknowledgments

This work was supported by the Centre National de la Recherche Scientifique (CNRS), Rennes Métropole, France, the Université de Rennes 1, France, Région Bretagne and the Fonds Européen de Développement Economique et Régional (FEDER).

- [1] J. C. G. Bünzli, C. Piguet, *Chem. Rev.* **2002**, *102*, 1897.
- [2] a) R. Sessoli, A. K. Powell, *Coord. Chem. Rev.* **2009**, *253*, 2328 and references cited therein; b) L. Sorace, C. Benelli, D. Gatteschi, *Chem. Soc. Rev.* **2011**, *40*, 3092, and references cited therein; c) C. Coulon, H. Miyasaka, R. Clerac, *Single-Molecule Magnets and Related Phenomena* (Ed.: R. Winpenny), Springer, Berlin, **2006**, p. 163.
- [3] J. D. Rinehart, M. Fang, W. J. Evans, J. R. Long, *Nat. Chem.* **2011**, *3*, 538.
- [4] a) M. N. Leuninger, D. Loss, *Nature* **2001**, *410*, 789; b) A. Ardavan, O. Rival, J. J. L. Morton, S. J. Blundell, A. M. Tyshkin, G. A. Timco, R. E. P. Winpenny, *Phys. Rev. Lett.* **2007**, *98*, 057201; c) P. C. E. Stamp, A. Gaita-Arino, *J. Mater. Chem.* **2009**, *19*, 1718.
- [5] A. Candini, S. Klyatskaya, M. Ruben, W. Wernsdorfer, M. Af fronte, *Nano Lett.* **2011**, *11*, 2634.
- [6] J. H. van Vleck, *J. Phys. Chem.* **1937**, *41*, 67.
- [7] a) J.-C. G. Bünzli, S. V. Eliseeva, *J. Rare Earths* **2010**, *28*, 824; b) J. Kido, Y. Okamoto, *Chem. Rev.* **2002**, *102*, 2347; c) M. D. McGehee, T. Bergstedt, C. Zhang, A. P. Saab, M. B. O'Regan, G. C. Bazan, V. I. Srdanov, A. J. Heeger, *Adv. Mater.* **1999**, *11*, 1349; d) A. de Bettencourt-Dias, *Dalton Trans.* **2007**, 2229.
- [8] a) J.-C. G. Bünzli, *Chem. Rev.* **2010**, *110*, 2729; b) C. P. Montgomery, B. S. Murray, E. J. New, R. Pal, D. Parker, *Acc. Chem. Res.* **2009**, *42*, 925; c) H. Tsukube, S. Shinoda, *Chem. Rev.* **2002**, *102*, 2389; d) S. Pandya, J. Yu, D. Parker, *Dalton Trans.* **2006**, 2757; e) R. M. Duke, E. B. Veale, F. M. Pfeffer, P. E. Kruger, T. Gunnlaugsson, *Chem. Soc. Rev.* **2010**, *39*, 3936; f) C. M. G. dos Santos, A. J. Harte, S. J. Quinn, T. Gunnlaugsson, *Coord. Chem. Rev.* **2008**, *252*, 2512; g) S. Shinoda, H. Tsukube, *Analyst* **2011**, *136*, 431; h) H. Tsukube, K. Yano, S. Shinoda, *Helv. Chim. Acta* **2009**, *92*, 2488.
- [9] a) V. W.-W. Yam, K. K.-W. Lo, *Coord. Chem. Rev.* **1999**, *184*, 157; b) J. Yuan, G. Wang, *TrAC Trends Anal. Chem.* **2006**, *25*, 490; c) G. Mathis, H. Bazin, in: *Lanthanide Luminescence* (Eds.: P. Hänninen, H. Härmä), Springer, Berlin, Heidelberg, **2010**, p. 1; d) E. G. Moore, A. P. S. Samuel, K. N. Raymond, *Acc. Chem. Res.* **2009**, *42*, 542.
- [10] a) J. Yuan, G. Wang, *J. Fluoresc.* **2005**, *15*, 559; b) A. Beeby, S. W. Botchway, I. M. Clarkson, S. Faulkner, A. W. Parker, D. Parker, J. A. G. Williams, *J. Photochem. Photobiol. B: Biology* **2000**, *57*, 83; c) G. Marriott, R. M. Clegg, D. J. Arndt-Jovin, T. M. Jovin, *Biophys. J.* **1991**, *60*, 1374.
- [11] a) S. V. Eliseeva, J.-C. G. Bünzli, in: *Springer Series on Fluorescence*, chapter 1, vol. 7, *Lanthanide Spectroscopy, Materials, and Bio-applications* (Eds.: P. Hänninen, H. Härmä), Springer, Berlin, vol. 7, **2010**; b) A. D'Aléo, F. Pointillart, L. Ouahab, C. Andraud, O. Maury, *Coord. Chem. Rev.* **2012**, *256*, 1604; c) S. V. Eliseeva, J.-C. G. Bünzli, *Chem. Soc. Rev.* **2010**, *39*, 189.
- [12] a) A. D'Aléo, A. Picot, A. Beeby, J. A. G. Williams, B. Le Guennic, C. Andraud, O. Maury, *Inorg. Chem.* **2008**, *47*, 10258; b) F. Pointillart, O. Maury, Y. Le Gal, S. Golhen, O. Cador, L. Ouahab, *Inorg. Chem.* **2009**, *48*, 7421; c) F. Pointillart, T. Cauchy, O. Maury, Y. Le Gal, S. Golhen, O. Cador, L. Ouahab, *Chem. Eur. J.* **2010**, *16*, 11926; d) F. Pointillart, A. Bourdolle, T. Cauchy, O. Maury, Y. Le Gal, S. Golhen, O. Cador, L. Ouahab, *Inorg. Chem.* **2012**, *51*, 978; e) A. Bourdolle, M. Allali, A. D'Aléo, P. L. Baldeck, K. Kamada, J. A. G. Williams, H. Le Bozec, C. Andraud, O. Maury, *ChemPhysChem* **2013**, *14*, 3361.
- [13] a) C. Andraud, O. Maury, *Eur. J. Inorg. Chem.* **2009**, 4357; b) A. D'Aléo, A. Picot, P. L. Baldeck, C. Andraud, O. Maury, *Inorg. Chem.* **2008**, *47*, 10269; c) A. D'Aléo, A. Bourdolle, S. Bulstein, T. Fauquier, A. Grichine, A. Duperray, P. L. Baldeck, C. Andraud, S. Brasselet, O. Maury, *Angew. Chem.* **2012**, *124*, 6726; *Angew. Chem. Int. Ed.* **2012**, *51*, 6622.
- [14] a) F. Pointillart, B. Le Guennic, S. Golhen, O. Cador, O. Maury, L. Ouahab, *Chem. Commun.* **2013**, *49*, 615; b) F. Pointillart, B. Le Guennic, T. Cauchy, S. Golhen, O. Cador, O. Maury, L. Ouahab, *Inorg. Chem.* **2013**, *52*, 5978.
- [15] a) G. Cucinotta, M. Perfetti, J. Luzon, M. Etienne, P.-E. Car, A. Caneschi, G. Calvez, K. Bernot, R. Sessoli, *Angew. Chem.* **2012**, *124*, 1638; *Angew. Chem. Int. Ed.* **2012**, *51*, 1606; b) M.-E. Boulon, G. Cucinotta, J. Luzon, C. Degl'Innocenti, M. Perfetti, K. Bernot, G. Calvez, A. Caneschi, R. Sessoli, *Angew. Chem.* **2013**, *125*, 368; *Angew. Chem. Int. Ed.* **2013**, *52*, 350; c) J. Long, R. Vallat, R. A. S. Ferreira, L. D. Carlos, F. A. A. Paz, Y. Guari, L. Larionova, *Chem. Commun.* **2012**, *48*, 9974.
- [16] G. Cosquer, F. Pointillart, S. Golhen, O. Cador, L. Ouahab, *Chem. Eur. J.* **2013**, *19*, 7895.
- [17] J. Wu, N. Dupont, S.-X. Liu, A. Neels, A. Hauser, S. Decurtins, *Chem. Asian J.* **2009**, *4*, 392.
- [18] M. Llunell, D. Casanova, J. Cirera, J. M. Bofill, P. Alemany, S. Alvarez, SHAPE (version 2.1), Barcelona, **2013**.
- [19] O. Kahn, *Molecular Magnetism*, VCH, Weinheim, Germany, **1993**.
- [20] A. Abragam, B. Bleaney, *Electron Paramagnetic Resonance of Transition Ions*, Dover Publications, New York, **1986**.
- [21] a) R. Orbach, *Proc. Phys. Soc. London Sect. A* **1961**, *264*, 458; b) C. Rudowicz, *J. Phys. C: Solid State Phys.* **1985**, *18*, 1415.
- [22] C. Görlder-Walrand, K. Binnemans, *Handbook on the Physics and Chemistry of Rare Earths*, **1996**, *23*, p. 121.
- [23] a) S. Faulkner, B. P. Burton-Pye, T. Khan, L. R. Martin, S. D. Wray, P. J. Skabara, *Chem. Commun.* **2002**, *16*, 1668; b) S. J. A. Pope, B. P. Burton-Pye, R. Berridge, T. Khan, P. J. Skabara, S. Faulkner, *Dalton Trans.* **2006**, 2907; c) T. Lazarides, M. A. H. Alamiry, H. Adams, S. J. A. Pope, S. Faulkner, J. A. Weinstein, M. D. Ward, *Dalton Trans.* **2007**, 1484.
- [24] a) W. D. Horrocks Jr., J. P. Bolender, W. D. Smith, R. M. Supkowski, *J. Am. Chem. Soc.* **1997**, *119*, 5972; b) R. M. Supkowski, J. P. Bolender, W. D. Smith, L. E. L. Reynolds, W. D. Horrocks Jr., *Coord. Chem. Rev.* **1999**, *185–186*, 307.

- [25] a) A. Beeby, S. Faulkner, J. A. G. Williams, *J. Chem. Soc., Dalton Trans.* **2002**, 1918; b) T. Lazarides, N. M. Tart, D. Sykes, S. Faulkner, A. Barbieri, M. D. Ward, *Dalton Trans.* **2009**, 3971.
- [26] D. Rehm, A. Weller, *Isr. J. Chem.* **1970**, 8, 259.
- [27] a) N. M. Shavaleev, S. J. A. Pope, Z. R. Bell, S. Faulkner, M. D. Ward, *Dalton Trans.* **2003**, 808; b) N. M. Shavaleev, L. P. Morcroft, S. J. A. Pope, Z. R. Bell, S. Faulkner, M. D. Ward, *Chem. Eur. J.* **2003**, 9, 5283; c) N. M. Shavaleev, G. Accorsi, D. Virgili, Z. R. Bell, T. Lazarides, G. Calogero, N. Armaroli, M. D. Ward, *Inorg. Chem.* **2005**, 44, 61; d) E. Di Piazza, L. Norel, K. Costuas, A. Bourdolle, O. Maury, S. Rigaut, *J. Am. Chem. Soc.* **2011**, 133, 6174.
- [28] a) J. Lemonnier, L. Guénée, C. Beuchat, T. A. Wesolowski, P. Mukherjee, D. H. Waldeck, K. A. Gogick, S. Petoud, C. Piguet, *J. Am. Chem. Soc.* **2011**, 133, 16219; b) L. Aboshyan-Sorgho, H. Nozary, A. Aebischer, J. G. Bünzli, P. Morgantini, K. R. Kittilstved, A. Hauser, S. V. Eliseeva, S. Petoud, C. Piguet, *J. Am. Chem. Soc.* **2012**, 134, 12674; c) N. M. Shavaleev, R. Scopelliti, F. Gumy, J.-C. G. Bünzli, *Inorg. Chem.* **2009**, 48, 2908; d) J. Zhang, P. D. Badger, S. J. Geib, S. Petoud, *Angew. Chem.* **2005**, 117, 2564; *Angew. Chem. Int. Ed.* **2005**, 44, 2508; e) N. M. Shavaleev, R. Scopelliti, F. Gumy, J.-C. G. Bünzli, *Inorg. Chem.* **2009**, 48, 2908; f) J. Zhang, P. D. Badger, S. J. Geib, S. Petoud, *Angew. Chem.* **2005**, 117, 2564; *Angew. Chem. Int. Ed.* **2005**, 44, 2508; g) C. Bischof, J. Wahsner, J. Scholten, S. Trosien, M. Seitz, *J. Am. Chem. Soc.* **2010**, 132, 14334.
- [29] a) C. Freund, W. Porzio, U. Giovannella, F. Vignali, M. Pasini, S. Destri, A. Mech, S. Di Pietro, L. Di Bari, P. Mineo, *Inorg. Chem.* **2011**, 50, 5417; b) A. Zaïm, H. Nozary, L. Guénée, C. Besnard, J.-F. Lemmonier, S. Petoud, C. Piguet, *Chem. Eur. J.* **2012**, 18, 7155.
- [30] F. R. Gonçalves Silva, O. L. Malta, C. Reinhard, H. U. Güdel, C. Piguet, J. Moser, J.-C. G. Bünzli, *J. Phys. Chem. A* **2002**, 106, 1670.
- [31] a) L. Ungur, S. K. Langley, T. N. Hooper, B. Moubaraki, E. K. Brechin, K. S. Murray, L. F. Chibotaru, *J. Am. Chem. Soc.* **2012**, 134, 18554; b) J. J. Le Roy, M. Jeletic, S. I. Gorelsky, I. Korobkov, L. Ungur, L. F. Chibotaru, M. Murugesu, *J. Am. Chem. Soc.* **2013**, 135, 3502; c) J. Ruiz, A. J. Mota, A. Rodríguez-Dieguez, S. Titos, J. M. Herrera, E. Ruiz, E. Cremades, J.-P. Costes, E. Colacio, *Chem. Commun.* **2012**, 48, 7916; d) F. Habib, J. Long, P.-H. Lin, I. Korobkov, L. Ungur, W. Wernsdorfer, L. F. Chibotaru, M. Murugesu, *Chem. Sci.* **2012**, 3, 2158; e) G. Novitchi, G. Pilet, L. Ungur, V. V. Moshchalkov, W. Wernsdorfer, L. F. Chibotaru, D. Luneau, A. K. Powell, *Chem. Sci.* **2012**, 3, 1169; f) S.-Y. Lin, W. Wernsdorfer, L. Ungur, A. K. Powell, Y.-N. Guo, J. Tang, L. Zhao, L. F. Chibotaru, H.-J. Zhang, *Angew. Chem.* **2012**, 124, 12939; *Angew. Chem. Int. Ed.* **2012**, 51, 12767; g) E. Bartolomé, J. Bartolomé, S. Melnic, D. Prodius, S. Shova, A. Arauzo, J. Luzon, F. Luis, C. Turta, *Dalton Trans.* **2013**, 42, 10153.
- [32] J.-L. Liu, K. Yuan, J.-D. Leng, L. Ungur, W. Wernsdorfer, F.-S. Guo, L. F. Chibotaru, M.-L. Tong, *Inorg. Chem.* **2012**, 51, 8538.
- [33] X. Lou, G. Zhang, I. Herrera, R. Kinach, O. Ornatsky, V. Baranov, M. Nitz, M. Winnik, *Angew. Chem.* **2007**, 119, 6223; *Angew. Chem. Int. Ed.* **2007**, 46, 6111.
- [34] a) C.-Y. Jia, S.-X. Liu, C. Tanner, C. Leiggener, L. Sanguinet, E. Levillain, S. Leutwyler, A. Hauser, S. Decurtins, *Chem. Commun.* **2006**, 1878; b) C. Jia, S.-X. Liu, C. Tanner, C. Leiggener, A. Neels, L. Sanguinet, E. Levillain, S. Leutwyler, A. Hauser, S. Decurtins, *Chem. Eur. J.* **2007**, 13, 3804.
- [35] M. F. Richardson, W. F. Wagner, D. E. Sands, *J. Inorg. Nucl. Chem.* **1968**, 30, 1275.
- [36] G. M. Sheldrick, *SHELX97 - Programs for Crystal Structure Analysis* (release 97-2), Institut für Anorganische Chemie der Universität, Tammanstrasse 4, 3400 Göttingen, Germany, **1998**; SIR97 - A. Altomare, M. C. Burla, M. Camalli, G. L. Casciarano, C. Giacovazzo, A. Guagliardi, A. G. G. Moliterni, G. Polidori, R. Spagna, *J. Appl. Crystallogr.* **1999**, 32, 115.
- [37] M. J. Frisch, G. W. Trucks, H. B. Schlegel, G. E. Scuseria, M. A. Robb, J. R. Cheeseman, G. Scalmani, V. Barone, B. Mennucci, G. A. Petersson, H. Nakatsuji, M. Caricato, X. Li, H. P. Hratchian, A. F. Izmaylov, J. Bloino, G. Zheng, J. L. Sonnenberg, M. Hada, M. Ehara, K. Toyota, R. Fukuda, J. Hasegawa, M. Ishida, T. Nakajima, Y. Honda, O. Kitao, H. Nakai, T. Vreven, J. A. Montgomery Jr., J. E. Peralta, F. Ogliaro, M. Bearpark, J. J. Heyd, E. Brothers, K. N. Kudin, V. N. Staroverov, R. Kobayashi, J. Normand, K. Raghavachari, A. Rendell, J. C. Burant, S. S. Iyengar, J. Tomasi, M. Cossi, N. Rega, J. M. Millam, M. Klene, J. E. Knox, J. B. Cross, V. Bakken, C. Adamo, J. Jaramillo, R. Gomperts, R. E. Stratmann, O. Yazyev, A. J. Austin, R. Cammi, C. Pomelli, J. W. Ochterski, R. L. Martin, K. Morokuma, V. G. Zakrzewski, G. A. Voth, P. Salvador, J. J. Dannenberg, S. Dapprich, A. D. Daniels, O. Farkas, J. B. Foresman, J. V. Ortiz, J. Cioslowski, D. J. Fox, *Gaussian 09*, revision A.02, Gaussian Inc., Wallingford CT, **2009**.
- [38] a) C. Adamo, V. Barone, *J. Chem. Phys.* **1999**, 110, 6158; b) M. Ernzerhof, G. E. Scuseria, *J. Chem. Phys.* **1999**, 110, 5029.
- [39] M. Dolg, H. Stoll, H. Preuss, *Theor. Chem. Acc.* **1993**, 85, 441.
- [40] F. Weigend, R. Ahlrichs, *Phys. Chem. Chem. Phys.* **2005**, 7, 3297.
- [41] a) G. Cosquer, F. Pointillart, B. Le Guennic, Y. Le Gal, S. Golhen, O. Cador, L. Ouahab, *Inorg. Chem.* **2012**, 51, 8488; b) F. Pointillart, B. Le Guennic, S. Golhen, O. Cador, O. Maury, L. Ouahab, *Inorg. Chem.* **2013**, 52, 1610; c) F. Pointillart, B. Le Guennic, O. Maury, S. Golhen, O. Cador, L. Ouahab, *Inorg. Chem.* **2013**, 52, 1398.
- [42] J. Tomasi, B. Mennucci, R. Cammi, *Chem. Rev.* **2005**, 105, 2999.
- [43] a) M. Cossi, V. Barone, *J. Chem. Phys.* **2001**, 115, 4708; b) R. Improta, V. Barone, G. Scalmani, M. J. Frisch, *J. Chem. Phys.* **2006**, 125, 054103.
- [44] A.-R. Allouche, *J. Comput. Chem.* **2011**, 32, 174.
- [45] F. Aquilante, L. De Vico, N. Ferre, G. Ghigo, P. A. Malmqvist, P. Neogady, T. B. Pedersen, M. Pitonak, M. Reiher, B. O. Roos, L. Serrano-Andres, M. Urban, V. Veryazov, R. Lindh, *J. Comput. Chem.* **2010**, 31, 224.
- [46] B. O. Roos, P. R. Taylor, P. E. M. Siegbahn, *Chem. Phys.* **1980**, 48, 157.
- [47] a) P.-Å. Malmqvist, B. O. Roos, *Chem. Phys. Lett.* **1989**, 155, 189; b) P.-Å. Malmqvist, B. O. Roos, B. Schimmelpfennig, *Chem. Phys. Lett.* **2002**, 357, 230.
- [48] L. F. Chibotaru, L. Ungur, *J. Chem. Phys.* **2012**, 137, 064112.
- [49] a) K. Andersson, P.-Å. Malmqvist, B. O. Roos, *J. Chem. Phys.* **1992**, 96, 1218; b) J. Finley, P.-Å. Malmqvist, B. O. Roos, L. Serrano-Andres, *Chem. Phys. Lett.* **1998**, 288, 299.

Received: October 21, 2013

Published Online: December 3, 2013